J. Non-Newtonian Fluid Mech. 157 (2009) 188–196

Contents lists available at ScienceDirect

Journal of Non-Newtonian Fluid Mechanics

journal homepage: www.elsevier.com/locate/jnnfm

Numerical stability of the method of Brownian configuration fields

Claude Mangoubi[a,b,*], Martien A. Hulsen[c], Raz Kupferman[a]

[a] Institute of Mathematics, The Hebrew University, Jerusalem 91904, Israel
[b] CERMICS, École Nationale des Ponts et Chaussées, 77455 Marne la Vallée, France
[c] Materials Technology, Eindhoven University of Technology, P.O. Box 513, 5600MB, Eindhoven, The Netherlands

ARTICLE INFO

Article history:
Received 29 July 2008
Received in revised form
13 November 2008
Accepted 14 November 2008

Keywords:
Brownian configuration fields
Finite element method
Flow around a cylinder
Numerical stability

ABSTRACT

We investigate numerical aspects of the Brownian configuration fields method, and in particular its numerical stability as the Weissenberg number increases. Our results show the method to be immune to the type of instability leading to numerical blowup in the simulation of macroscopic models. We discuss this finding in the light of the stability criterion proposed in Fattal et al. [R. Fattal, R. Kupferman, Time-dependent simulation of viscoelastic flows at high Weissenberg using the log-conformation representation, J. Non Newtonian Fluid Mech. 126 (2005) 23–37].

1. Introduction

A major obstacle in the computation of polymeric fluid dynamics has been the so-called high Weissenberg number problem (HWNP). This term refers to the numerical breakdown of computations beyond a certain range of the Weissenberg number, Wi , where the precise onset of this breakdown depends on the model, on the geometry, and on the numerical scheme. For time-dependent computations this breakdown is usually manifested in a numerical blowup of the solution, i.e., a numerical instability. For steady-state computations it is usually manifested in a lack of convergence. Virtually all macroscopic models have been reported to suffer from this numerical breakdown [12].

Recent progress has been made with the introduction of the "log-conformation" transformation (log-C) [5]. It was realized that the presence of exponential profiles in the stress tensor, formed by the combination of stress advection and stress stretching, imposes a severe stability restriction on the spatial mesh size. This restriction becomes particularly pronounced in the vicinity of stagnation points. The log-conformation method consists in replacing the constitutive equation for the conformation tensor C by an evolution equation for its matrix logarithm, $\log C$ (in most macroscopic models, the conformation tensor is symmetric positive-definite, therefore has a well-defined matrix logarithm). The balance between advection and deformation no longer imposes a stability constraint on the spatial mesh when solving the new equations for $\log C$. The log-C formulation has been implemented with finite differences [5,6], finite elements [9,13], and finite volume methods [1] for various constitutive equations and several geometries. In all cases, it has resulted in significant improvement over previous computations: the numerical instability either vanished or was deferred to very high values of Wi. It is to be noted however, that the log-C method loses accuracy at large Wi.

In the 1990s so-called micro–macro models were introduced. In the micro–macro approach, the conservation laws of mass and momentum remain in the form of macroscopic equations for the velocity and pressure fields. The macroscopic constitutive equation for the stress, however, is replaced by a stochastic system of equations for variables that represent, in some coarse-grained sense, the fluctuating polymers. A Kramers formula links between the two scales, relating the stochastic variables to the macroscopic stress field. Whilst such methods are expensive computationally, they offer evident advantages: the model has a clear physical meaning, and the stochastic equation is easy to discretize. Two numerical implementations of the micro–macro approach are the CONNFFESSIT method of Öttinger and co-worker [14] and the method of Brownian Configuration Fields (BCF) of Hulsen et al. [10]. In CONNFFESSIT, the polymers are represented by particles that are advected with the flow, i.e., it is a Lagrangian method. In BCF, the conformation of the polymers is represented by a spatially continuous field, which makes it suitable for traditional schemes based on spatial discretization, hence can be represented by either Lagrangian or Eulerian formulations. The general expe-

* Corresponding author at: Institute of Mathematics, The Hebrew University, Jerusalem 91904, Israel. Tel.: +972 2 658 4159; fax: +972 2 563 0702.
E-mail addresses: claude.mangoubi@gmail.com (C. Mangoubi), m.a.hulsen@tue.nl (M.A. Hulsen), raz@math.huji.ac.il (R. Kupferman).

0377-0257/$ – see front matter © 2008 Elsevier B.V. All rights reserved.
doi:10.1016/j.jnnfm.2008.11.009

rience is that micro–macro methods are more robust than their macroscopic counterparts [10,11]. A natural question is: what is the source of this robustness? In particular, are micro–macro methods sensitive to the numerical instability pointed out in [12], and if they are, does a logarithmic transformation of variables improve stability?

The present paper studies numerical aspects of the BCF method as Wi grows to values of $O(1)$ and beyond. Extended simulations are performed for the finitely-extensible nonlinear elasticity (FENE) kinetic model, in which each polymer molecule is treated as a nonlinear dumbbell. The chosen geometry is flow around a confined cylinder; while there are no geometric singularities here, two stagnation points are present at the front and back of the cylinder, which is where computations usually fail. We display results for Weissenberg numbers in the range $[0, 5]$ and maximum elongation parameter, b, of 50 and higher. We also run simulations for the Hookean dumbbell model, in which we are able to reach a value of $\mathrm{Wi} = 1.6$ without numerical divergence. We explain the robustness of the BCF in the light of the stability criterion proposed in [6]. According to this criterion, the BCF method is intrinsically better conditioned than macroscopic methods, due to a smaller factor in front of the stretching term. Another part of this work is the implementation of a logarithmic transformation of the dumbbell's extension vector, to check whether stability can be improved further. However, in agreement with our stability analysis, this transformation does not improve the stability. Lastly, we emphasize that even though the BCF method is immune to the numerical instability described in [12], the solutions in the wake of the cylinder do not converge upon mesh refinement for Wi large enough.

2. The BCF method and its numerical implementation

2.1. Background

We now introduce the BCF method. Throughout this paper we work within the creeping flow regime. The macroscopic equations of momentum and mass conservation are:

$$\begin{aligned} &-\nabla p + \eta_s \Delta \boldsymbol{u} + \nabla \cdot \boldsymbol{\tau} = 0 \\ &\nabla \cdot \boldsymbol{u} = 0, \end{aligned} \tag{1}$$

where $\boldsymbol{u} = \boldsymbol{u}(t, \boldsymbol{x})$ is the velocity field, $p = p(t, \boldsymbol{x})$ is the pressure field, $\tau = \tau(t, \boldsymbol{x})$ is the extra-stress tensor, and the constant η_s is the solvent viscosity. The extra-stress τ is obtained from a kinetic model of the form

$$\begin{aligned} &\boldsymbol{\tau} = \frac{\eta_p}{\lambda} \left(\langle \boldsymbol{q} \otimes \boldsymbol{F}(\boldsymbol{q}) \rangle - \boldsymbol{I} \right) \\ &\mathrm{d}\boldsymbol{q}_t + (\boldsymbol{u} \cdot \nabla \boldsymbol{q}) \, \mathrm{d}t = \left(\kappa \boldsymbol{q} - \frac{1}{2\lambda} \boldsymbol{F}(\boldsymbol{q}) \right) \mathrm{d}t + \frac{1}{\sqrt{\lambda}} \mathrm{d}\boldsymbol{W}_t, \end{aligned} \tag{2}$$

where $\kappa = (\nabla \boldsymbol{u})^T$. The random function $\boldsymbol{q} = \boldsymbol{q}(t, \boldsymbol{x})$ is called the configuration field—it models the extension vector of the polymers. The function $\boldsymbol{F}(\boldsymbol{q})$ is the internal force exerted by a polymer in state $\boldsymbol{q}$, and $\boldsymbol{W} = \boldsymbol{W}(t)$ is a Wiener process. The parameter η_p is the polymeric viscosity, whereas λ is a typical relaxation time of the fluid. The Weissenberg number is defined as $\mathrm{Wi} = \frac{\lambda U}{a}$, where U and a are a typical velocity and length of the problem. The model is endowed with boundary conditions, which in the case of a bounded domain, Ω, consist of impermeable no-slip boundaries.

The stochastic *partial* differential Eq. (2) models a stochastic process in a space of functions on Ω. This stochastic equation induces an evolution on the probability density $\psi(\boldsymbol{q}, \boldsymbol{x}, t)$ of finding at position $\boldsymbol{x}$ and time t the polymers in state $\boldsymbol{q}$; the density ψ satisfies a Fokker–Planck equation. Expectations with respect to ψ are denoted by

$$\langle f(\boldsymbol{q}) \rangle = \int_{\mathbb{R}^3} f(\boldsymbol{q}) \psi(\boldsymbol{q}, \boldsymbol{x}, t) \, \mathrm{d}\boldsymbol{q}.$$

In Brownian simulations, the solution $\boldsymbol{q}(t, \boldsymbol{x})$ to (2) is simulated by N random functions $\boldsymbol{q}_j(t, \boldsymbol{x})$, $j = 1, \ldots, N$, which are approximations to N independent realizations of $\boldsymbol{q}(t, \boldsymbol{x})$. Each of the $\boldsymbol{q}_j$ satisfies (2) with an independent Brownian noise $\boldsymbol{W}_j(t)$. The stress $\boldsymbol{\tau}$, which is given by an expectation with respect to $\boldsymbol{q}(t, \boldsymbol{x})$ is approximated by an ensemble average

$$\boldsymbol{\tau} = \frac{\eta_p}{\lambda} \left[\frac{1}{N} \sum_{j=1}^{N} \boldsymbol{q}_j \otimes \boldsymbol{F}(\boldsymbol{q}_j) - \boldsymbol{I} \right],$$

i.e., $\boldsymbol{\tau}$ is a stochastic process as well. As a result, the velocity $\boldsymbol{u}$ which is obtained by solving the Stokes system (1) is random, hence the coupling between the processes $\boldsymbol{q}_j$. Another quantity with physical meaning is the conformation tensor, given by $\boldsymbol{C} = \langle \boldsymbol{q} \otimes \boldsymbol{q} \rangle$ and approximated by the ensemble average $\frac{1}{N} \sum_{j=1}^{N} \boldsymbol{q}_j \otimes \boldsymbol{q}_j$.

For the dumbbell spring force $\boldsymbol{F}$ we use the FENE dumbbell model

$$\boldsymbol{F}(\boldsymbol{q}) = \frac{\boldsymbol{q}}{1 - |\boldsymbol{q}|^2 / b},$$

where b is the maximum value that $|q|^2$ is allowed to assume (the maximum elongation parameter). The macroscopic variables $\boldsymbol{u}$, p and $\boldsymbol{\tau}$ are given in dimensional units, whereas $\boldsymbol{q}$ and $\boldsymbol{F}$ are scaled such that $\langle \boldsymbol{q} \otimes \boldsymbol{F} \rangle = \boldsymbol{I}$ in the absence of flow.

The BCF method was first presented and implemented in [10] for the Hookean dumbbell model (which coincides with the FENE model with $b = \infty$). At low Wi, results were in agreement with computations with the equivalent macroscopic Oldroyd-B model. Results were also displayed for values of Wi for which the macroscopic computations break down, indicating that BCF is more robust than its macroscopic counterpart. The BCF method was also implemented for the FENE and FENE-P models in [11], but only for small Weissenberg numbers. Other authors have since implemented this method ([3,8]), but its numerical stability as Wi increases has not yet been investigated.

2.2. An implicit-in-time BCF scheme

An obstacle to computing at higher Weissenberg numbers (e.g., [11]) is the time discretization of the stochastic differential Eq. (2). The simplest discretization is the forward-Euler method: denoting the discrete-in-time approximation of $\boldsymbol{q}(\boldsymbol{x}, t_n)$ by $\boldsymbol{q}^n(\boldsymbol{x})$, the scheme is

$$\boldsymbol{q}^{n+1} = \boldsymbol{q}^n + \left(-\boldsymbol{u}^n \cdot \nabla \boldsymbol{q}^n + \kappa^n \boldsymbol{q}^n - \frac{1}{2\lambda} \boldsymbol{F}(\boldsymbol{q}^n) \right) \Delta t + \frac{1}{\sqrt{\lambda}} \Delta \boldsymbol{W}^n,$$

where $\boldsymbol{u}^n(\boldsymbol{x}) = \boldsymbol{u}(\boldsymbol{x}, t_n)$, $\boldsymbol{\kappa}^n(\boldsymbol{x}) = (\nabla \boldsymbol{u}^n)^T(\boldsymbol{x})$, and $\Delta \boldsymbol{W}^n$ is a normally distributed variable with expectation 0 and variance Δt.

In the case of the FENE force, this scheme very quickly leads to an over-extension of the dumbbells. This means that the updated value $\boldsymbol{q}^{n+1}$ is such that $|\boldsymbol{q}^{n+1}|^2 > b$, which violates the model. This can be remedied by reducing the time-step, but for moderately large λ the restriction on the time step becomes so stringent that it makes it an impractical solution. An alternative is to use an implicit-in-time discretization, for example, Öttinger's predictor-corrector method [15]. We use a simpler implicit discretization, which is the backward Euler scheme with only the spring force term treated implicitly. This leads to the following equation for $\boldsymbol{q}^{n+1}$:

$$\boldsymbol{q}^{n+1} + \frac{1}{2\lambda} \boldsymbol{F}(\boldsymbol{q}^{n+1}) \Delta t = \boldsymbol{q}^n + \left(-\boldsymbol{u}^n \cdot \nabla \boldsymbol{q}^n + \kappa^n \boldsymbol{q}^n \right) \Delta t + \frac{1}{\sqrt{\lambda}} \Delta \boldsymbol{W}^n$$

For the FENE force

$$\left(1+\frac{1}{2\lambda}\frac{\Delta t}{1-|\boldsymbol{q}^{n+1}|^2/b}\right)\boldsymbol{q}^{n+1}=\boldsymbol{D}(\boldsymbol{u}^n,\boldsymbol{q}^n,\Delta\boldsymbol{W}^n)\equiv\boldsymbol{D}^n,$$

where

$$\boldsymbol{D}(\boldsymbol{u},\boldsymbol{q},\Delta\boldsymbol{W})=\boldsymbol{q}+(-\boldsymbol{u}\cdot\nabla\boldsymbol{q}+\kappa\boldsymbol{q})\,\Delta t+\frac{1}{\sqrt{\lambda}}\Delta\boldsymbol{W}$$

is given at the current time step. Taking absolute values of both sides, denoting the magnitude of any vector v by v, results in a cubic equation for q^{n+1},

$$(q^{n+1})^3-D^n(q^{n+1})^2-b\left(1+\frac{\Delta t}{2\lambda}\right)q^{n+1}+bD^n=0.$$

Following Öttinger, it can be shown that there is only one root which satisfies $q^{n+1}<\sqrt{b}$. Defining

$$a_1=-D^n\qquad a_2=-b\left(1+\frac{\Delta t}{2\lambda}\right)\qquad a_3=bD^n$$

$$p=\frac{3a_2-a_1^2}{9}\qquad r=\frac{9a_1a_2-27a_3-2a_1^3}{54}\qquad \theta=\arccos\left(\frac{r}{\sqrt{-p^3}}\right),$$

the unique root satisfying $q^{n+1}<\sqrt{b}$ is

$$q^{n+1}=2\sqrt{-p}\cos\left(\frac{\theta+4\pi}{3}\right)-\frac{a_1}{3}$$

The updated vector $\boldsymbol{q}^{n+1}$ is now recovered with

$$\boldsymbol{q}^{n+1}=\left(1+\frac{1}{2\lambda}\frac{\Delta t}{1-(q^{n+1})^2/b}\right)^{-1}\boldsymbol{D}^n.$$

3. Numerical results

3.1. Problem setting

We consider planar flow past a confined cylinder. The cylinder has radius $a=1$, and is positioned at the center of a channel of width $2H$, where $H=2a$. The total length of the flow domain is $30a$. The geometry is depicted in Fig. 1.

We impose periodic conditions at the inflow and outflow boundaries. We assume reflection symmetry across the channel axis, hence we only compute in half of the domain, and impose zero tangential traction along the center-line. The flow is driven by a constant flow rate Q, so that the average velocity across the channel is $U=Q/2H=1$ and the Weissenberg number is $\mathrm{Wi}=\lambda$. The

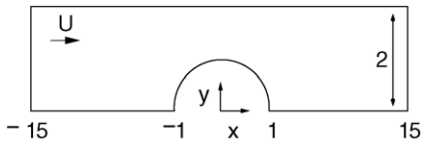

Fig. 1. Geometric setting of the flow problem.

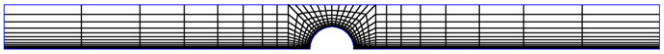

Fig. 2. mesh1.

Table 1
Mesh parameters.

	$n1$	$n2$	$n3$	$n4$	δ	Number of elements
mesh1	8	8	12	6	0.02161	480
mesh2	8	12	16	6	0.01459	784
mesh3	12	16	18	10	0.01101	1104
mesh4	16	16	24	12	0.01101	1920

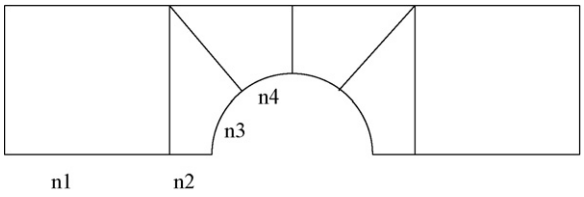

Fig. 3. Mesh parameters used in the cylinder problem.

fluid parameters are $\eta_s=0.59$ and $\eta_p=0.41$. In most calculations the maximum elongation is $b=50$. The value of $b=100$ is also used to allow comparison with results in [9] for the Giesekus model with mobility parameter $\alpha=0.01$.

We use four different meshes, denoted from coarsest to finest by mesh1 to mesh4. The coarsest mesh is shown in Fig. 2. Specifications for the four meshes are given in Table 1. The parameters n_i are the number of elements along a curve as shown in Fig. 3. The parameter δ measures the shortest dimension of the smallest radial element. All our computations use a finite elements scheme with the DEVSS/DG stabilization. More details can be found in [10].

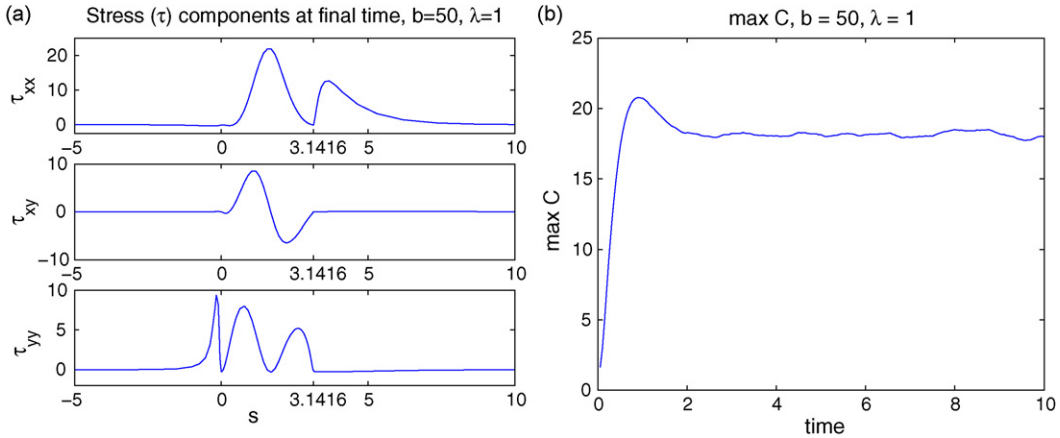

Fig. 4. (a) Snapshot of the $\boldsymbol{\tau}$ components on the center-line and along the cylinder wall at $t=10$ (τ_{zz} is not shown, as it is very small compared to the other components). (b) Evolution of the maximal conformation component $c(t)$ given by (3). The parameters are $b=50$, $\lambda=1$, $\Delta t=10^{-2}$ and $N=5000$.

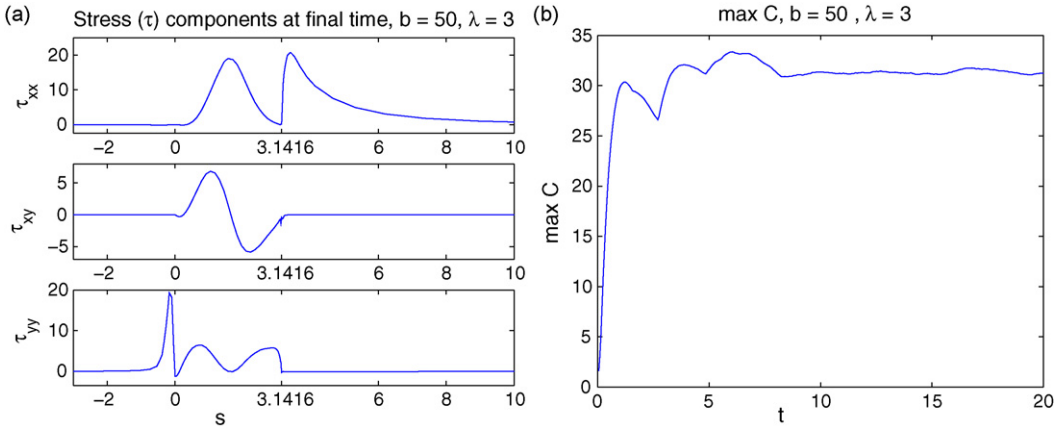

Fig. 5. (a) Snapshot of the $\boldsymbol{\tau}$ components on the center-line and around the cylinder at $t = 20$. (b) Evolution of the maximal conformation component (3). The parameters are $b = 50$, $\lambda = 3$, $\Delta t = 10^{-2}$, and $N = 5000$.

3.2. Low Wi

We first show results using the coarsest mesh at relatively low Weissenberg number, $\lambda = 1$. We would like to examine the results when the macroscopic values reach steady-state in a statistical sense, which requires solving the system for a sufficiently long time interval. It is commonly accepted that a time interval of length at least 5λ is necessary. The results which are displayed in Fig. 4 are for a time interval of $10\lambda = 10$.

In Fig. 4 a we show the three components of the stress tensor τ_{xx}, τ_{xy} and τ_{yy} on the center-line and along the cylinder wall at the final time. The s-axis corresponds to arclength along the lower boundary of the integration domain. The range $0 \leq s \leq \pi$ corresponds to the cylinder wall, while $s < 0$ and $s > \pi$ correspond to arclength along the center line, in front of and behind the cylinder, respectively. We make the following observations:

τ_{xx}: There are two peaks, the highest of which is in the vicinity of the cylinder wall, approximately at the top, $s = \pi/2$, where shearing is strongest because it is tangent to the wall. A weaker peak is observed in the wake; it is due to the elongation of the polymers right behind the rear stagnation point. At the rear stagnation point itself, the dynamics are at equilibrium and $\tau_{xx} \simeq 0$ (theoretically it should be 0).

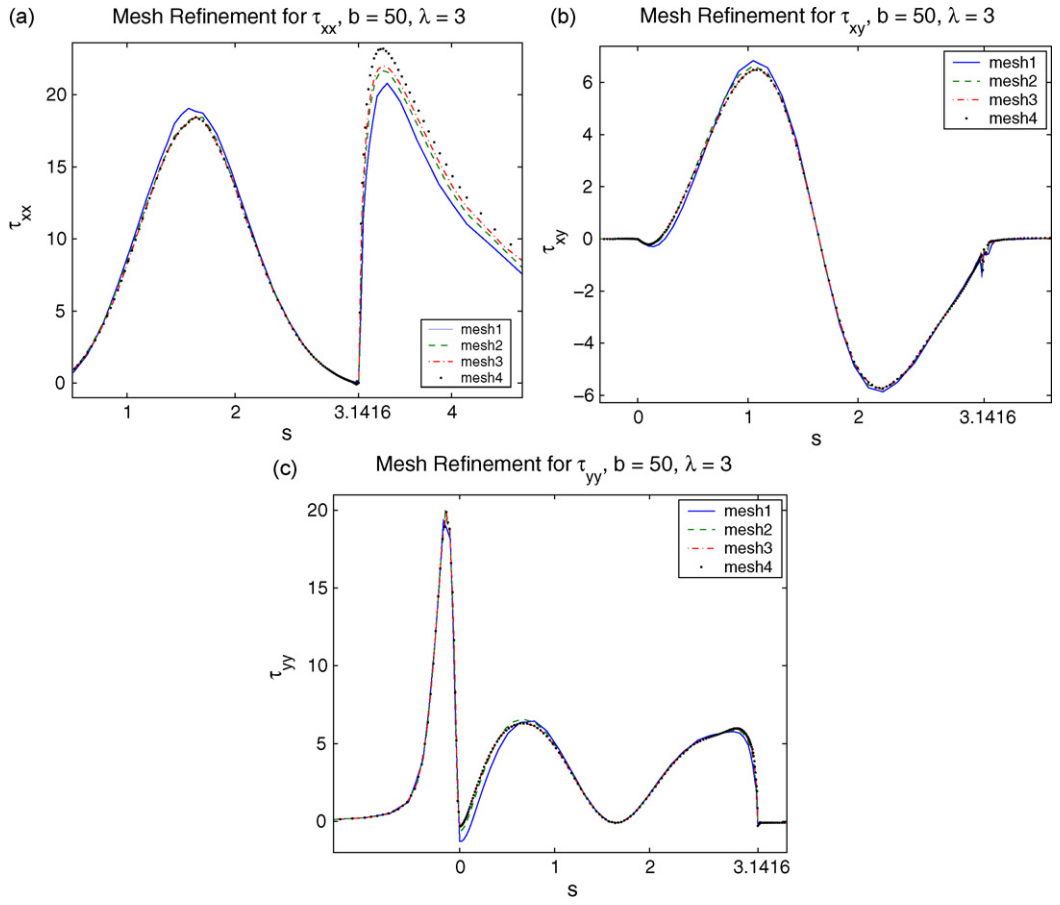

Fig. 6. Snapshot of τ_{xx}, τ_{xy} and τ_{yy} at the center-line and around the cylinder at $t = 20.5$ for four different meshes. The parameters are $b = 50$, $\lambda = 3$, $\Delta t = 10^{-2}$ and $N = 5000$.

τ_{xy}: Two extremal values of opposite signs are reached at the cylinder wall, near the points $s = \pi/4$ and $s = 3\pi/4$. τ_{xy} changes signs at $s = \pi/2$. The second peak is smaller in amplitude. There is nothing visible in the wake, where elongation occurs (theoretically τ_{xy} should be 0).

τ_{yy}: A first peak is formed at the front of the cylinder due to the strong elongation dynamics just before the stagnation point; τ_{yy} then drops to nearly 0 at the stagnation point (again, theoretically it should be 0). Two additional peaks form on the side of the cylinder; as for τ_{xy}, the second peak is weaker.

In Fig. 4 b we show the time evolution of the maximum of the largest component of $\boldsymbol{C}$ over the whole domain

$$c(t) = \max_{\boldsymbol{x}\in\Omega}\max_{i,j}|C_{ij}(t,\boldsymbol{x})|. \tag{3}$$

The transient overshoot is due to the shearing peak on the cylinder visible in τ_{xx}. It develops very fast, and eventually relaxes. The fluctuations are due to the stochasticity, they decrease when the number of fields N increases.

3.3. Higher Weissenberg

We next raise the Weissenberg number to $\lambda = 3$. The time interval is 20, which should suffice to reach steady-state. In this computation, we also refined the mesh to check for convergence upon mesh refinement. In Fig. 5 a, the components of the stress tensor are displayed and in Fig. 5 b the evolution of the maximal conformation component (3) is shown. The main differences with the $\lambda = 1$ results are:

(a) In early stages, the largest peak in τ_{xx} develops near the cylinder wall, but eventually τ_{xx} reaches its maximum value in the wake. This type of behavior is visible in Fig. 5 b; the first peak is due to overshooting in C_{xx} next to the cylinder wall, the second to overshooting in C_{yy} before the stagnation point in front of the cylinder, and the last one to overshooting in C_{xx} in the wake. The wake region is also much more extended than for Wi = 1.
(2) A discontinuity in τ_{xy} forms just before the rear stagnation point at $s = \pi$. The same discontinuity has been observed in [4]; its origin is not clear.
(3) The peak in τ_{yy} at the front of the cylinder is now comparable in size to the largest peak in τ_{xx}.
(4) The two peaks in the vicinity of the cylinder wall in components τ_{xy}, τ_{yy} have become closer in amplitude.

In Fig. 6 a we show a magnified graph of τ_{xx} in the regions where it reaches its maxima for the four meshes. Convergence upon mesh refinement can be seen at the peak near the cylinder wall. In contrast, there is no convergence in the wake. This lack of convergence has been observed before in the simulation of macroscopic models. Interestingly, the two other components of $\boldsymbol{\tau}$ seem to converge (see Fig. 6 b and c), even though the maximum value of τ_{yy} at the front of the cylinder is of the same order as the maximum value of τ_{xx} in the wake.

We have run simulations at larger values of Wi , up to Wi = 7. The trends observed for $\lambda = 3$ are even stronger. The peak in τ_{xx} in the wake becomes much larger than the peak at the cylinder wall. The discontinuity in τ_{xy} becomes more pronounced and the peak in τ_{yy} becomes larger than the peak in τ_{xx}. At Wi = 7, we even observe non-steady behavior in τ_{yy} at the front of the cylinder. It is not clear whether this is a real bifurcation or a numerical artifact.

3.4. Larger b

For $b = 50$, no instability similar to what is known in the macroscopic models has been observed. We increased b in order to allow the dumbbells larger extension values. This should be more favorable to the development of exponential profiles characterized in [6].

For a FENE model having a large value of b, the elongational-to-shear viscosity ratio equals $2b$. For the Giesekus model, this ratio is equal to $2/\alpha$. By choosing $b = 100$, we can then compare our results to [9], where flow of a Giesekus fluid with $\alpha = 0.01$ is computed. There, with the same physical parameters and geometry, it is found that the critical value for the Wi number beyond which numerical divergence occurs is 1.2. Here, we found a much higher threshold; until Wi = 6, there was no breakdown. Since the two models are so different (the FENE model is not a stochastic equivalent of the Giesekus model), the comparison can only be indicative of an improved stability of the BCF method compared to macroscopic methods. For Wi = 7, the computations break down.

For $b = 1000$ simulations were found to be stable up to Wi = 2. At Wi = 3, the computations break down. At this point, it is unclear whether this can be circumvented or whether the breakdown is really a consequence of the formation of exponential profiles in the dumbbells.

3.5. Results for a Hookean dumbbell fluid

We have also simulated the flow of a Hookean dumbbell fluid (the microscopic counterpart of an Oldroyd-B fluid) around a confined cylinder (Fig. 7). It was noticed already in [10] that the BCF model in this case seems more robust than the corresponding macroscopic model. While in macroscopic simulations, the critical Weissenberg number for which computations break down is about 0.9 in this geometrical setting, we reach a value of 1.6 without numerical divergence, but with very large errors. Here we show a simulation for Wi = 1, where the result is still smooth. We note that the threshold value of Wi = 1.6 is similar to the one found in [9] for the breakdown of the Oldroyd-B model using the log-C method (in the same setting exactly).

4. The log-BCF transformation

4.1. A logarithmic transformation applied to the BCF method

As mentioned in the introduction, an interesting question is whether a logarithmic type of transformation applied to the dumbbells would improve the stability of the BCF method. The original log-C transformation was applied to the conformation tensor, which in our context corresponds to the average $\langle \boldsymbol{q}\otimes\boldsymbol{q}\rangle$. Here, we need to adapt this idea to a transformation of the Brownian fields. There are numerous possible choices: we transform the magnitude of the elongation q and leave unchanged its orientation, defining a new Brownian field:

$$\boldsymbol{w} = \frac{f(q)}{q}\boldsymbol{q} \qquad f(q) = \log(1+q).$$

Note that $w = \log(1+q)$, so that $w = 0$ if and only if $q = 0$. An equation for $\boldsymbol{w}(t,\boldsymbol{x})$ is derived through Itô's formula [7]. If a vectorial stochastic process $\boldsymbol{x}(t)$ in $\mathbb{R}^n$ satisfies an SDE

$$\mathrm{d}\boldsymbol{x}_t = \boldsymbol{a}\mathrm{d}t + \boldsymbol{B}\mathrm{d}\boldsymbol{W}_t$$

where $\boldsymbol{a}\in\mathbb{R}^n$, $\boldsymbol{B}\in\mathbb{R}^{n\times n}$, then the stochastic process $\boldsymbol{y} = \boldsymbol{g}(\boldsymbol{x})$ satisfies the SDE

$$\mathrm{d}\boldsymbol{y}_t = \left(\boldsymbol{a}\cdot\nabla\boldsymbol{g} + \frac{1}{2}\boldsymbol{B}\boldsymbol{B}^T : \nabla\nabla\boldsymbol{g}\right)\mathrm{d}t + (\nabla\boldsymbol{g})^T\boldsymbol{B}\mathrm{d}\boldsymbol{W}_t.$$

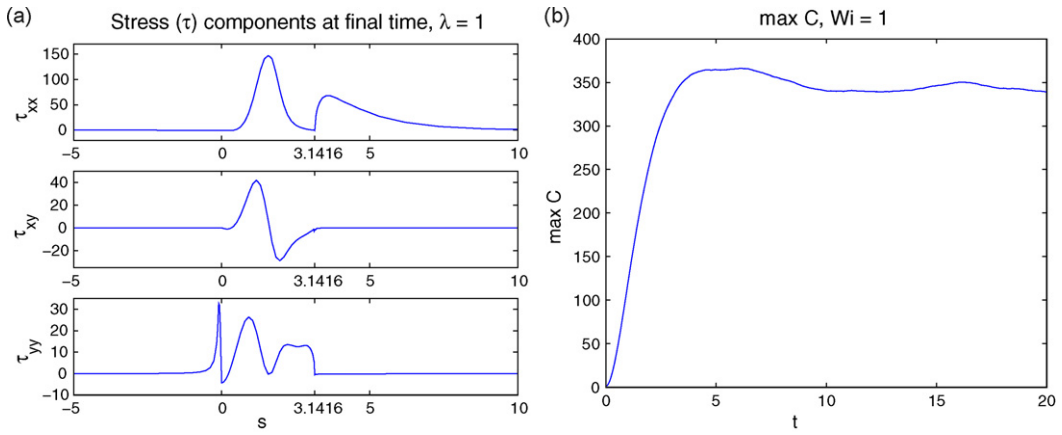

Fig. 7. Hookean dumbbell: (a) Snapshot of the $\boldsymbol{\tau}$ components at the center-line and around the cylinder at $t = 20$. (b) Evolution of the maximal conformation component (3). The parameters are $\lambda = 1$, $\Delta t = 10^{-2}$ and $N = 5000$.

Applying this to $\boldsymbol{w}$ we get

$$\begin{aligned} \mathrm{d}\boldsymbol{w}_t + (\boldsymbol{u}\cdot\nabla\boldsymbol{w})\,\mathrm{d}t &= \left(\frac{f'(q)}{q^2}\left(\boldsymbol{q}^T\boldsymbol{\kappa}\boldsymbol{q}\right)\boldsymbol{q} + \frac{w}{q}\left(\boldsymbol{I} - \frac{\boldsymbol{q}\boldsymbol{q}^T}{q^2}\right)\boldsymbol{\kappa}\boldsymbol{q} - \frac{1}{2\lambda}f'(q)\boldsymbol{F}\right)\mathrm{d}t \\ &+ \left(\frac{1}{2\lambda}\left(f''(q) + \frac{2f'(q)}{q} - \frac{2w}{q^2}\right)\frac{\boldsymbol{q}}{q}\right)\mathrm{d}t \\ &+ \frac{1}{\sqrt{\lambda}}\left[f'(q)\frac{\boldsymbol{q}\boldsymbol{q}^T}{q^2} + \frac{w}{q}\left(\boldsymbol{I} - \frac{\boldsymbol{q}\boldsymbol{q}^T}{q^2}\right)\right]\mathrm{d}\boldsymbol{W}_t, \end{aligned} \tag{4}$$

where we have used both $\boldsymbol{q}$, $\boldsymbol{w}$ variables to avoid writing exponentials and logarithms. We have used the fact that if the vector $\boldsymbol{q}$ is convected with the flow, then so is the vector $\boldsymbol{w}$. We can interpret the first deterministic term on the right-hand side as stretching, the second as rotation, the third as relaxation, and the fourth is an additional drift term arising from second moments of the noise. This is similar to the log-C transformation, where the flow deformation $\boldsymbol{\kappa}$ is decomposed into pure stretching and pure rotation. We note that the same stochastic differential equation can be obtained by a derivation similar to the one in [5] for the log-C transformation.

As in the regular BCF case, we expect over-extension to occur here as well. To prevent this we can use an implicit in time scheme as before, by making the spring force implicit:

$$\left(\boldsymbol{w}^{n+1} + \frac{1}{2\lambda}f'(q^{n+1})\frac{\boldsymbol{q}^{n+1}}{1-(q^{n+1})^2/b}\right)\Delta t = \boldsymbol{D}(\boldsymbol{u}^n, \boldsymbol{q}^n, \boldsymbol{w}^n, \Delta\boldsymbol{W}^n) \equiv \boldsymbol{D}^n,$$

where

$$\begin{aligned} \boldsymbol{D}(\boldsymbol{u},\boldsymbol{q},\boldsymbol{w},\Delta\boldsymbol{W}) &= \left[-\boldsymbol{u}\cdot\nabla\boldsymbol{w} + \frac{f'(q)}{q^2}\left(\boldsymbol{q}^T\boldsymbol{\kappa}\boldsymbol{q}\right)\boldsymbol{q} + \frac{w}{q}\left(\boldsymbol{I} - \frac{\boldsymbol{q}\boldsymbol{q}^T}{q^2}\right)\boldsymbol{\kappa}\boldsymbol{q}\right]\Delta t \\ &+ \frac{1}{2\lambda}\left(f''(q) + \frac{2f'(q)}{q} - \frac{2w}{q^2}\right)\frac{\boldsymbol{q}}{q}\,\Delta t \\ &+ \frac{1}{\sqrt{\lambda}}\left[f'(q)\frac{\boldsymbol{q}\boldsymbol{q}^T}{q^2} + \frac{w}{q}\left(\boldsymbol{I} - \frac{\boldsymbol{q}\boldsymbol{q}^T}{q^2}\right)\right]\Delta\boldsymbol{W}. \end{aligned}$$

Again, we take the absolute values of both sides and obtain an algebraic equation for $z = q^{n+1}$:

$$g(z) = \left(1 + z - \frac{z^2}{b} - \frac{z^3}{b}\right)\left[\log(1+z) - D^n\right] + \frac{\Delta t}{2\lambda}z = 0.$$

Here we need to use an iterative method to find the appropriate root. In order to prevent solutions with $z > \sqrt{b}$, we look for the roots of the function $h(x) = g(x)(1-(x^2/b))^{-1}$, which has the same roots as $g(x)$ and diverging asymptotes at $x = \sqrt{b}$. We use a Newton solver, with the additional precaution that if an iterate exceeds $\sqrt{b}$ we set it to the value of $\sqrt{b} - \epsilon$ for some small value of ϵ.

4.2. Numerical results for the log-BCF transformation

For low values of Wi the results are very similar to those obtained in Section 3 without the logarithmic transformation. However, a slight difference already exists at the values of $b = 50$, $\lambda = 1$. The log-BCF method predicts a slightly lower value for the peak in τ_{xx} in the wake than the regular BCF method. We ran simulations for the large value of $\lambda = 5$. The log-BCF method seems quite stable, however comparison of the two methods shows a larger discrepancy in the wake.

In Fig. 8 a, we compare the profiles of τ_{xx} with the two formulations. As expected from the $\lambda = 3$ case, the peak in the wake is larger than the peak around the cylinder, in the BCF computation. The log-BCF computation, however, predicts smaller values in the wake. The wake is now very extended and does not decay to the equilibrium value at the end of the computational domain. This means we are solving in practice a flow around a periodic array of confined cylinders. Comparisons of the two other stress components reveal only small differences in the vicinity of the peaks.

We have also increased the maximum extension parameter b to values of 100 and 1000. We were able to reach values of $\lambda = 5$ and $\lambda = 2$, respectively, without numerical breakdown. This is similar to our findings for the regular BCF method.

A natural question is whether the BCF method is more or less accurate than the log-transformed BCF. At the moment, we do not know the answer. We note, however, that since the log-BCF method is of order one half in time, it may be less accurate. In order to check this, we have run two simulations with a reduced time-step of $\Delta t = 5 \times 10^{-3}$, in both the Wi = 3 and Wi = 5 cases. Our findings do not lead to a clear conclusion; in the Wi = 3 case, reducing the time-step does not change the results significantly. In the Wi = 5 case, however, the reduced time-step computation predicts a significantly higher value of τ_{xx} in the wake, which is even higher than what the regular BCF predicts.

4.3. The Hookean dumbbells case

We implemented our logarithmic transformation with the Hookean dumbbells. We witnessed a slight improvement, as we were able to reach Wi = 1.8 without numerical blow-up, but still with large errors.

5. A theoretical stability criterion

In this section we shed some light on the remarkable stability properties of the BCF method, compared to its macroscopic coun-

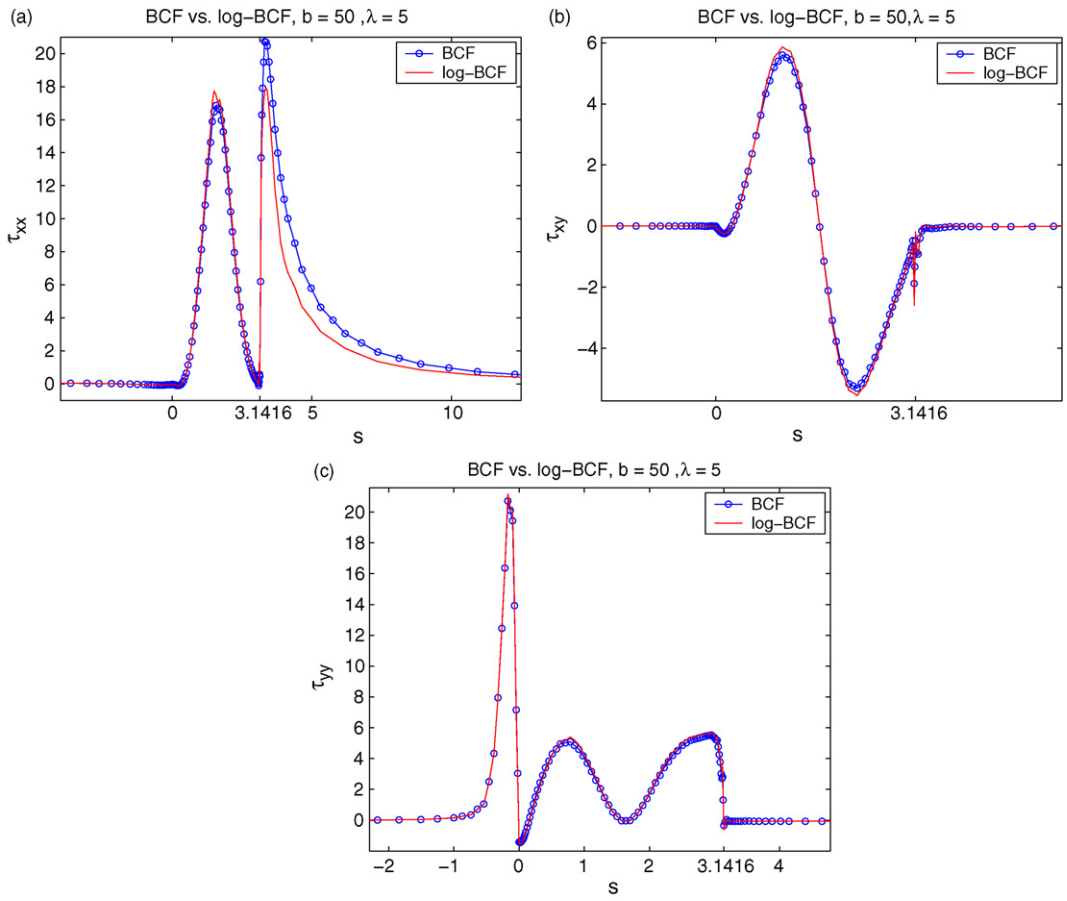

Fig. 8. Snapshots of τ_{xx}, τ_{xy} and τ_{yy} at the center-line and around the cylinder at $t = 48$, for both the BCF and the logarithmic BCF. The parameters are $\lambda = 5$, $\Delta t = 10^{-2}$ and $N = 5000$.

terparts. For example, macroscopic computations of an Oldroyd-B fluid around a confined cylinder break down, without the log-C regularization, at a Weissenberg number of about 0.9. The BCF solution of the corresponding Hookean dumbbell model only breaks down at Wi ≈ 1.6. One important difference between the two approaches is that BCF preserves the positive definiteness of the conformation tensor, whereas positive definiteness may be violated in macroscopic simulations. Yet, even though the breakdown of macroscopic simulations is often accompanied by the loss of positive definiteness, it has been shown [9], at least for the confined cylinder geometry, that the breakdown occurs precisely at the Weissenberg number where the "stability criterion" presented in [6] is violated. The question we try to answer is whether BCF is better conditioned with respect to this stability criterion.

The stability criterion in [6] was derived by analyzing a simple scalar equation in one space dimension that mimics the interplay between advection, stretching and relaxation. Let us consider the following toy-Oldroyd-B model

$$\frac{\partial \phi}{\partial t} + u\frac{\partial \phi}{\partial x} = 2u'\phi - \frac{1}{\lambda}\phi, \tag{5}$$

where $x \in [0, 1]$, $u(x)$ is given, and $u(x)$, $u'(x)$ are assumed positive. We choose the boundary and initial condition for $\phi(t, x)$ arbitrarily to be $\phi(t, 0) = 1$, $t > 0$ and $\phi(0, x) = 1$. Here ϕ is analogous to C_{xx} and u and u' are analogous to the velocity field and its gradient. The factor of 2 in front of the $u'\phi$ term arises from the upper convected derivative.

Under mild restrictions on $u(x)$, the solution to (5) reaches a steady state irrespectively of initial conditions. Yet, if we discretize it with, say, a first-order upwind scheme,

$$\phi_j^{n+1} = \phi_j^n - \frac{u_j \Delta t}{\Delta x}(\phi_j^n - \phi_{j-1}^n) + \Delta t \left(2u_j' - \frac{1}{\lambda}\right)\phi_j^n,$$

we see that the solution ϕ_j^n remains bounded, as $n \to \infty$, only if

$$1 - \frac{u_j \Delta t}{\Delta x} + \Delta t \left(2u_j' - \frac{1}{\lambda}\right) \le 1,$$

i.e., if

$$2u_j' - \frac{1}{\lambda} \le \frac{u_j}{\Delta x}.$$

If λ is sufficiently small such that $\lambda \le 1/2u_j'$ for all j, then this condition is trivially satisfied. For points where $2u_j' > 1/\lambda$ the mesh size Δx has to satisfy the stability condition

$$\Delta x \le \frac{u_j}{2u_j' - 1/\lambda}.$$

In order to evaluate the velocity gradient, we use an upwind approximation for u', so that at each point

$$u_j' = \frac{u_j - u_{j-1}}{\Delta x}.$$

Suppose now that the first point is a stagnation point, with $u_0 = 0$, then

$$u_1' = \frac{u_1}{\Delta x},$$

so the stability condition becomes:

$$\mathrm{Wi}_1 := \frac{\lambda u_1}{\Delta x} \leq 1, \tag{6}$$

where Wi_1 is a "numerical Weissenberg number" at the first cell after the stagnation point.

The corresponding toy model that mimics BCF is

$$\mathrm{d}\phi_t + u\frac{\partial \phi}{\partial x}\mathrm{d}t = \left(u'\phi - \frac{1}{2\lambda}\phi\right)\mathrm{d}t + \frac{1}{\sqrt{\lambda}}\mathrm{d}W_t. \tag{7}$$

The notable difference with (5), except for the presence of a stochastic forcing, is that the stretching term here is smaller by a factor of 2. The upwind scheme takes the form

$$\phi_j^{n+1} = \left[1 - \frac{u_j \Delta t}{\Delta x} + \left(u_j' - \frac{1}{2\lambda}\right)\Delta t\right]\phi_j^n + u_j\frac{\Delta t}{\Delta x}\phi_{j-1}^n + \frac{\Delta W_j}{\sqrt{\lambda}}.$$

The stability condition preventing the appearance of exponential profiles now becomes

$$u_j' - \frac{1}{2\lambda} \leq \frac{u_j}{\Delta x}.$$

Again, if λ is sufficiently small such that $\lambda \leq 1/2u_j'$, this condition is trivially satisfied. Otherwise, using as before an upwind approximation for u', the stability condition is trivially satisfied for $\mathrm{Wi}_1 \geq 0$.

Let us comment on the above analysis in the light of the actual computations. Firstly, condition (6) concerns Wi_1, which can be related qualitatively to Wi by the following argument. As observed in [9], the velocity gradient behind the stagnation point is overestimated, at least in the meshes considered; in Fig. 9 one can see that $\lambda u' \sim O(1)$, regardless of the mesh size. Thus, Wi_1 and Wi are of the same order, and (6) really sets a critical Wi. Secondly, the factor of two that arises from the upper convected derivative changes radically the stability of the equations, instead of causing a scaling of the critical Weissenberg number. While this simple analysis shows the toy-BCF to be immune to the instability occurring in the toy-Oldroyd-B, it can only give a hint with regards to the full two-dimensional models, where the same type of analysis is more complicated. Indeed, the breakdown which eventually occurs in the simulation of Hookean dumbbells is not predicted here. Moreover, the stability condition (6) depends on the numerical approximation used; some numerical methods may remain unstable.

The above discussion indicates why the BCF method is in general more stable than macroscopic models. In our specific example of the FENE force implementation however, this stability is improved further by the implicit scheme applied to the nonlinear force term. We have found no clear stability criterion for a toy-FENE model, since the equation for ϕ_j^{n+1} is cubic and not linear anymore.

Turning now to the logarithmic type transformation applied to the dumbbells, it seems less surprising that no major improvement in stability is visible, as the implicit FENE scheme is already very robust. In the case of the Hookean dumbbells, we have witnessed a slight improvement but basically the critical Wi number remains of the same order. We can try to explain this using again a toy model. Let us define $\psi = \log(1+\phi)$ where ϕ is the (positive) solution of

$$\frac{\partial \phi}{\partial t} + u\frac{\partial \phi}{\partial x} = u'\phi - \frac{1}{2\lambda}\phi, \quad \phi(t=0,x) = \phi(t,x=0) = \varepsilon > 0,$$

(for simplicity we consider a deterministic version of (7)). Then ψ is a solution of the transformed equation

$$\frac{\partial \psi}{\partial t} + u\frac{\partial \psi}{\partial x} = \left(u' - \frac{1}{2\lambda}\right)\left(1 - e^{-\psi}\right)$$
$$\psi(t=0,x) = \psi(t,x=0) = \log(1+\varepsilon) > 0.$$

Writing as before an upwind scheme for ψ:

$$\psi_j^{n+1} = \psi_j^n\left(1 - u\frac{\Delta t}{\Delta x}\right) + \Delta t\left(u' - \frac{1}{2\lambda}\right)\left(1 - e^{-\psi_j^n}\right) + u\frac{\Delta t}{\Delta x}\psi_{j-1}^n, \tag{8}$$

we note that at startup, when ψ_j^n is small, we can use the approximation $e^{\psi_j^n} \approx 1 + \psi_j^n$, to obtain:

$$\psi_j^{n+1} = \left[1 - u\frac{\Delta t}{\Delta x} + \left(u' - \frac{1}{2\lambda}\right)\Delta t\right]\psi_j^n + u\frac{\Delta t}{\Delta x}\psi_{j-1}^n.$$

This means we would have to impose exactly the same condition on the grid size as without the transformation in order to prevent exponential growth. This is different from the log-C method, where the stability criterion vanishes totally. In our case, if the condition on Δx is not enforced, we might reach highly inaccurate values for ψ_j^n. At this point the transformation becomes useful, since then $e^{-\psi_j^n} \ll 1$, and (8) is approximated by

$$\psi_j^{n+1} = \psi_j^n\left(1 - u\frac{\Delta t}{\Delta x}\right) + \left(u' - \frac{1}{2\lambda}\right)\Delta t + u\frac{\Delta t}{\Delta x}\psi_{j-1}^n,$$

for which there are no restrictions on the grid size. Of course, we have prevented blowup at the cost of losing accuracy, which may be the cause for the numerical failure eventually observed in the log transformation applied to the Hookean dumbbells.

6. Discussion and conclusion

We have shown, through numerical computations, the BCF method to be immune to the type of instability observed in macroscopic models as the Weissenberg number grows to values of $O(1)$. This is especially striking in the case where the dumbbell internal spring force is nonlinear, as in the FENE example. We have also implemented a logarithmic type of transformation of the BCF field in order to check whether it improved stability, as in the log-C transformation in the macroscopic case. Stability remains essentially unchanged, both in the FENE and Hookean dumbbell cases.

Analyzing two simple toy-models, we have gained insight into the remarkable stability of the BCF model. We argue that the main reason is the reduction of the stretching term by a factor of two compared to the macroscopic models. To support this claim, we have also tested macroscopic models in which the stretching term was artificially reduced (results not shown). These simulations also exhibited much better stability properties. These findings resolve a misconception whereby the BCF model is often thought to be stable due to the inherent positive-definiteness of the conformation tensor. Although this might help also, we showed that its stability should be mainly understood in the light of the stability condition discovered in [6].

Even though the BCF method seems much more stable than its macroscopic counterparts, it suffers from a lack of convergence upon mesh refinement in problematic areas of the geometrical setting (in our case, at the wake of the cylinder). It also remains unclear why the method eventually breaks down.

Acknowledgments

RK and CM were partially supported by the Israel Science Foundation. Part of this research was done while CM stayed at the Université de Montréal, Canada and at the CERMICS, ENPC, France. We thank the referees for useful comments.

References

[1] A. Alfonso, M. A. Alves, F. T. Pinho, P.J. Oliveira, The log-conformation tensor approach in the FVM framework: benchmark solutions and stability analysis, IWNMNNF 2007.

[3] C. Chauvière, A. Lozinski, Simulation of complex viscoelastic flows using the Fokker-Planck equation: 3D FENE model, J. Non-Newtonian Fluid Mech. 122 (2004) 201–214.
[4] Y. Fan, H. Yang, R.I. Tanner, Stress boundary layers in the viscoelastic flow past a cylinder in a channel: limiting solutions, Acta Mech. Sin. 21 (2005) 311–321.
[5] R. Fattal, R. Kupferman, Constitutive laws for the matrix-logarithm of the conformation tensor, J. Non-Newtonian Fluid Mech. 123 (2004) 281–285.
[6] R. Fattal, R. Kupferman, Time-dependent simulation of viscoelastic flows at high Weissenberg number using the log-conformation representation, J. Non-Newtonian Fluid Mech. 126 (2005) 23–37.
[7] C.W. Gardiner, A Handbook of Stochastic Methods, Springer, Berlin, Heidelberg, 2004.
[8] X. Hu, Z. Ding, L.J. Lee, Simulation of 2D transient viscoelastic flow using the CONNFESSIT approach, J. Non-Newtonian Fluid Mech. 127 (2005) 107–122.
[9] M.A. Hulsen, R. Fattal, R. Kupferman, Flow of viscolelastic fluids past a cylinder at high Weissenberg number: stabilized simulations using matrix logarithms, J. Non-Newtonian Fluid Mech. 127 (2005) 27–39.
[10] M.A. Hulsen, A.P.G. van Heel, B.H.A.A. van den Brule, Simulation of viscoelastic flows using Brownian configuration fields, J. Non-Newtonian Fluid Mech. 70 (1997) 79–101.
[11] A.P.G. van Heel, M.A. Hulsen, B.H.A.A. van den Brule, On the selection of parameters in the FENE-P model, J. Non-Newtonian Fluid Mech. 75 (1998) 253–271.
[12] R. Keunings, Simulation of viscoelatic fluid flow, in: C.L. Tucker III (Ed.), Fundamentals of Computer Modeling for Polymer Processing, Carl Hanser Verlag, 1989, pp. 402–470.
[13] Y. Kwon, Finite element analysis of planar 4:1 contraction flow with tensor-logarithmic formulation of differential constitutive equations, Korea-Aust. Rheol. J. 16 (2004) 183–191.
[14] M. Laso, H.C. Öttinger, Calculation of viscoelastic flow using molecular models: the connffessit approach, J. Non-Newtonian Fluid Mech. 47 (1993) 1–20.
[15] H.C. Öttinger, Stochastic Processes in Polymeric Fluids, Springer, 1996.